

# 1 DIODEM – A Diverse Inertial and Optical Dataset of 2 kinEmatic chain Motion

3 Simon Bachhuber<sup>1,\*</sup>, Dustin Lehmann<sup>2</sup>, Ive Weygers<sup>1</sup>, and Thomas Seel<sup>3</sup>

4 <sup>1</sup>FAU Erlangen-Nürnberg, Department Artificial Intelligence in Biomedical Engineering, Erlangen, 91052, Germany

5 <sup>2</sup>Technische Universität Berlin, Control Systems Group, Berlin, 10587, Germany

6 <sup>3</sup>Leibniz Universität Hannover, Institute of Mechatronic Systems, Hannover, 30167, Germany

7 \*corresponding author: Simon Bachhuber (simon.bachhuber@fau.de)

## 8 ABSTRACT

Real-world applicability and adoption of inertial motion tracking technology depends on the development of advanced algorithms that overcome challenges like magnetometer-free and sparse sensing, sensor-to-segment alignment, and motion artifact reduction. This publication and the accompanying dataset foster this development by providing researchers with the ability to systematically study and explore various combinations of these challenges in a well-controlled setting. The dataset comprises 46 minutes of optical and inertial data (20 reflective markers and ten, rigidly and foam-attached IMUs) of five-segment kinematic chains that feature different joint types and are moved in a large indoor tracking range such that they perform motions of various speeds and characteristics. Due to the large number of segments, as well as the different types of joints, motions, and sensor attachments, this dataset allows researchers to identify and push the boundaries of current inertial motion tracking solutions and to develop and validate novel methods for application areas ranging from biomechanics to autonomous systems.

## 10 Background & Summary

Numerous engineering applications require precise tracking of articulated bodies in Kinematic Chains (KCs). Notable examples include: Unobtrusive tracking of human motions outside laboratory environments<sup>1,2</sup>, integrating with robotic systems in immersive industrial or clinical environments<sup>3</sup> and creating real-time feedback mechanisms in rehabilitation<sup>4</sup>, and aerial robotics<sup>5</sup>. In all of these and many more applications, inertial measurement units (IMUs) play a crucial role for their ability to estimate the complete pose of KCs – providing a cost-effective and reliable alternative to state-of-the-art multi-camera and marker-less<sup>6,7</sup> alternatives that constantly require line of sight.

Recent developments have significantly enhanced the practical application potential of Inertial Motion Tracking (IMT) by addressing several inherent challenges: Firstly, the accuracy of orientation estimation has been substantially improved through the adoption of neural network-based approaches<sup>8</sup> and advanced complementary filter structures<sup>9</sup>. Secondly, most indoor environments exhibit a disturbed magnetic field<sup>10,11</sup>, which has led to the development of numerous joint-specific magnetometer-free motion tracking solutions<sup>12–14</sup>. Furthermore, application-specific solutions have been proposed to achieve plug-and-play sensor-to-segment alignment<sup>15–17</sup>, and assignment<sup>18–20</sup>.

Although many solutions are available for specific IMT challenges underlying a practical use-case, to truly advance IMT in real-world applications, solutions for combinations of IMT challenges need to be developed. Furthermore, real-world applicability of IMT calls for several additional vastly understudied IMT challenges, such as sparse sensing<sup>21–23</sup> (where fewer sensors than segments are employed) and effective strategies for mitigating artifacts (caused by the nonrigid attachment of sensors relative to the bone due to soft-tissue motion)<sup>24,25</sup>. Combining IMT challenges is still largely unexplored, and addressing them holistically could significantly impact the practical deployment and effectiveness of IMT.

The growing number of recently published datasets that include inertial sensors underscores the expanding interest in this area. This includes datasets, focused on specific use cases in human motion tracking<sup>26–31</sup> and datasets that bring novel measurement modalities<sup>32–36</sup> to the forefront. However, these datasets involve skin-attached sensors and human kinematics which introduce inaccuracies in the ground truth kinematics due to soft-tissue motion, errors in sensor-to-segment alignment, and human joint inaccuracies unless markers are drilled to the bone<sup>36</sup>, and that these effects can be entangled inseparably. Compared with these datasets, the dataset proposed here is designed to catalyze further advancements in IMT by utilizing a mechanical setup which allows for a controlled environment with accurately known kinematics and ground truth, and well-calibrated sensor attachments. To the best of our knowledge, there exists only a single dataset<sup>37</sup> that also uses a mechanical setup. It uses a motor-driven double-hinge-joint three-segment KC that performs a limited number of swinging motions and excludes all forms of global KC translation and/or rotation. In contrast, the proposed dataset offers long five-segment KCs interconnected by hinge-, saddle-, and spherical joints with rigidly and foam-attached IMUs that performs motions of various

40 speeds and characteristics including global KC translation and/or rotation. Due to the large number of segments, as well as the  
41 different types of joints, motions, and sensor attachments, a large variety of fundamental underlying Inertial Motion Tracking  
42 Problems (IMTPs) and combinations of IMT challenges can be created such as, e.g., different kinematic structures and lengths,  
43 Degrees of Freedom (DoF), and number of sensors; including the ability to modify levels of sparseness and introduce motion  
44 artifacts. Additionally, we provide easy-to-use functions to define specific IMTPs tailored to the envisioned use-case. Overall,  
45 this results in a large set of valuable real-world IMTPs that can be systematically studied and solved in a controlled environment,  
46 thus evaluating the practical applicability of inertial sensors in diverse settings and applications.

## 47 Methods

48 In this section, we describe the experimental setup and the recorded data. Specifically, we first outline the measurement setup,  
49 then describe the measurement protocol – including the sequence of actions that are performed – and then the variables that are  
50 altered in order to create a set of different experiments. Finally, we describe the processing that is applied to all experimental  
51 recordings.

### 52 Measurement Setup

53 In all experiments, a 3D-printed five-segment KC moves in space (see Figure 1). We have recorded the motion of two five-  
54 segment KCs that differ in the types of joints used. The first KC, titled arm, consists of three hinge joints, each oriented along  
55 the z, y, and x axes, respectively, followed by a spherical joint. The second KC, titled gait, consists of a sequence of y-hinge,  
56 saddle, saddle, and y-hinge joints. The majority of the parts of the KC are 3D-printed using PLA on a Prusa MK4 printer. The  
57 joints use additional off-the-shelf hardware such as bearings for smooth movement. The CAD files are made available<sup>38</sup>. For  
58 both KCs, all segments are of equal physical dimensionality and only differ in their coloring and marker-attachment side beams.

59 To each segment in both five-segment KCs, two IMUs and four Optical Motion Capture (OMC) markers are attached. The  
60 two wireless IMUs per segment (Mtw Awinda, Xsens, Enschede, the Netherlands) record 3D acceleration, angular velocity, and  
61 magnetic field density at a sampling rate of 40 Hertz. One IMU is attached rigidly to a 3D-printed fixture. The second IMU is  
62 attached nonrigidly to the segment via foam, see Figure 2. During recording, all ten IMUs, comprising two units per segment  
63 across five segments, wirelessly transmit their data to a host PC using proprietary software. Note that both IMUs are attached  
64 such that the IMU's sensing x-axis aligns with the axial/longitudinal direction of the segment, and in a way that both IMUs are  
65 aligned with the segment's coordinate system as defined by the OMC markers.

66 Four OMC markers are rigidly attached either directly to each segment, or on 3D-printed beams that point orthogonal  
67 to the segment's longitudinal direction. For each segment, the four markers are placed specifically to allow for simple and  
68 robust calculation of an orthogonal coordinate system. A minimum of three non-collinear markers are necessary to establish a  
69 coordinate system, but four markers per segment were used to reduce registration errors from occlusion in the optical motion  
70 tracking system. The 3D position of all 20 markers (five segments, four markers per segment) are tracked using an OMC system  
71 (OptiTrack Prime 22, NaturalPoint, Inc., Corvallis, U.S.A.) with an array of twelve cameras and at a sampling rate of 30 Hertz.

72 Additionally, video recordings were obtained using two high-definition cameras (OptiTrack Prime Color) from two different  
73 angles for transparent documentation, understanding and referencing of the applied measurement protocol.

### 74 Measurement Protocol

75 For both five-segment KCs several experiments have been performed. An experiment corresponds to a type (or several types of)  
76 motion(s) that are sequentially performed in one continuous recording session. For each experiment, the data was obtained  
77 through the following actions: 1) The two synchronized cameras start recording; 2) The ten synchronized IMUs start recording;  
78 3) The OMC starts recording (20 synchronized markers are tracked); 4) The five-segment KC rests for 30 seconds (this enables  
79 the users to perform bias estimation and removal if desired, or to validate such methods); 5) The five-segment KC moves in  
80 space; 6) The OMC stops recording; 7) The ten IMUs stop recording simultaneously; 8) The two cameras stop recording  
81 simultaneously.

### 82 Measurement Variables

83 In total, eleven experiments are obtained. Each experiment uses the hardware and the measurement protocol as described above.  
84 Recall that each experiment consists of a five-segment KC that is manipulated by two human motion tracking experts to create  
85 a sequence of motions, e.g., the KC *arm* performs first 30 seconds of slow random motion, then pause for ten seconds, and  
86 continue and finish the experiment with 30 seconds of fast random motion. The wording of slow and fast motion is here used to  
87 identify the type of motion. The eleven experiments are created by varying the five-segment KC between the arm and gait chain,  
88 and by varying the sequence of types of motion between qualitatively distinctive types of motion. The types of joints of the two  
89 KCs have been chosen to allow for motion that is inspired by upper-body pick-and-place motion and by lower-body gait-like  
90 motion, respectively. The types of motions are classified as motion without pattern (random motion) and with pattern. For both

91 of these types of motion, the excitation level is varied from standstill up to very fast motion. Additionally, distinctive types  
92 of motion, such as seesawing or shaking, are recorded. Regarding motions with pattern, distinctive types of motion, such as  
93 pick-and-place and gait-like motion, are recorded. Moreover, a large number of types of motions are recorded in two variations,  
94 once where the KC is undergoing large amounts of (global) translation, and once where the amount of (global) translation is  
95 minimized. Overall, the following types of motions are recorded:

- 96 • Canonical: Excite all DoF of the KC consecutively, as decoupled as possible, at approximately one-second intervals. For  
97 example, a hinge joint is moved across its entire range of motion spectrum in about one second. Then there is a short  
98 pause and the next joint is excited.
- 99 • Freeze: The KC remains as still as possible for a few seconds (less than three seconds) and is “frozen” in motion.
- 100 • Pause: The KC rests on the table and is at a complete standstill.
- 101 • Slow: The KC is slowly moved randomly in space and all DoF are excited as evenly as possible. The KC is not  
102 deliberately moved and rotated globally in space.
- 103 • Fast: The KC is quickly moved randomly in space and all DoF are excited as evenly as possible. The KC is not  
104 deliberately moved and rotated globally in space.
- 105 • Dangle: The KC is only held at one segment and hangs downwards. This segment is moved and the rest of the KC  
106 follows physically and is in free fall.
- 107 • Global: The KC is deliberately moved and rotated globally in space.
- 108 • Shaking: The KC is not rotated but rather quickly translated by shaking the KC.
- 109 • Pick-and-place: The KC is moved such that it mimics arm motion that performs a pick-and-place task.
- 110 • Gait: The KC is moved such that it mimics the motion of the lower-body during gait. Gait-like motion is performed to  
111 achieve a faster or a slower gait.
- 112 • Quasi-static: The KC is very slowly moved randomly in space and all DoF are excited. The KC is not deliberately moved  
113 and rotated globally in space.

## 114 Data Processing

115 All experiments are processed using the same pipeline that includes the following steps:

- 116 1. Replacing NaN values in the marker trajectories obtained from the OMC system using cubic interpolation. This method  
117 ensured that the data remained consistent and accurate for further analysis.
- 118 2. Time-synchronization of inertial and optical data by cropping of initial inertial data. This is because, as specified in the  
119 measurement protocol, the IMUs starts recording before the OMC system starts recording. The cutoff point is found  
120 using the method as proposed in<sup>39</sup> which relies on cross-correlation of calculated (OMC data) and measured (IMU data)  
121 angular velocities.
- 122 3. Matching data dimensions, by cropping inertial data to match the (now synchronized) optical data.
- 123 4. Construction of an orthogonal body coordinate system  $\mathcal{B}$  using the four marker trajectories for each segment. Figure 3  
124 shows the different local coordinate systems and reference coordinate systems. This is done by first estimating the plane  
125 that is spanned by the four OMC markers (to this end, at least three markers are required; must be available and not  
126 NaN). Afterwards, the cross product is used to find the normal direction of the plane. Then, from the plane information  
127 (x-y-plane) and normal direction (z-direction) an orthogonal coordinate system  $\mathcal{B}$  that aligns with the respective sensor  
128 coordinate system  $\mathcal{S}$  is constructed.
- 129 5. Correction of any misalignment errors between the local sensor coordinate system  $\mathcal{S}$  and the body coordinate system of  
130 the respective segment  $\mathcal{B}$  which has been constructed by the OMC marker trajectories in the previous step. This is done  
131 by optimizing for a sensor-to-segment rotation such that the rigidly-attached IMU measurements match a virtual IMU that  
132 follows the OMC coordinate system. This method is further outlined in<sup>39</sup>. The determined sensor-to-segment rotation is  
133 then used to transform all IMU measurements from the local sensor coordinate system  $\mathcal{S}$  to the body coordinate system  
134  $\mathcal{B}$ .

135     6. Alignment of the earth reference coordinate system  $\mathcal{E}$  and the OMC reference coordinate system  $\mathcal{M}$ . The OMC system  
136     records the marker trajectories in an internal, arbitrary reference coordinate system  $\mathcal{M}$ . Consequently, the constructed  
137     body coordinate system  $\mathcal{B}$  captures the orientation of the segment relative to the OMC's reference coordinate system  
138      $\mathcal{M}$ . However, the IMUs measures the magnetic field and gravity vector which are defined relative to the earth reference  
139     coordinate system  $\mathcal{E}$ . In this last preprocessing step, we compute the constant rotation between OMC's reference  
140     coordinate system  $\mathcal{M}$  and earth reference coordinate system  $\mathcal{E}$ . This computation is performed simultaneously with the  
141     optimization of the previous step. This method is outline in detail in<sup>39</sup>. The determined rotation between the reference  
142     coordinate systems is then used to transform all 3D marker trajectories and body coordinate systems from  $\mathcal{M}$  to  $\mathcal{E}$ .

143     For more comprehensive details regarding these preprocessing steps and the software implementations utilized, readers are  
144     referred to the study by<sup>39</sup>. The data processing software is made openly available<sup>38</sup>.

## 145     Data Records

146     The data records are hosted in the following repository:

147                 <https://doi.org/10.7910/DVN/SGJLZA><sup>38</sup>

148     They include 1) the (processed) dataset, 2) associated videos of the experiments and images of the KCs, 3) the corresponding  
149     raw data and data processing software and tools employed, and 4) the CAD files for 3D-printing the KCs. The subsequent  
150     subsections are structured accordingly. The folder structure of the data records is visualized in Figure 4.

### 151     Processed Dataset /dataset/\*

152     The dataset is contained in the folder /dataset/\*. It contains optical and inertial data of a five-segment KC moving in space.  
153     There exist two different five-segment KCs, namely arm and gait. For both KCs, each experiment is a sequence of several  
154     types of motions motionY, and several experiments expX (in total eleven, E01 to E11) are obtained by varying the types of  
155     motion that are performed. The total lengths of the eleven experiments are given in Table 1, and the dataset folder structure is  
156     visualized in Figure 4.

157     For each experiment expX and motion motionY there are three files:

- 158         • expX\_motionY\_imu\_nonrigid.csv: The accelerometer, gyroscope, and magnetometer measurements of five IMUs  
159         where each IMU is *nonrigidly* attached to the respective segment. These measurements are expressed in the respective  
160         body coordinate system  $\mathcal{B}$ .
- 161         • expX\_motionY\_imu\_rigid.csv: The accelerometer, gyroscope, and magnetometer measurements of five IMUs,  
162         where each IMU is *rigidly* attached to the respective segment. These measurements are expressed in the respective body  
163         coordinate system  $\mathcal{B}$ .
- 164         • expX\_motionY\_omc.csv: For each of the five segments, the trajectories of four 3D marker positions expressed in  
165         coordinates of the earth reference coordinate system  $\mathcal{E}$ , and the trajectory of quaternions that encodes the orientation of  
166         the segment's body coordinate system relative to the earth reference coordinate system.

167     For both expX\_motionY\_imu\_nonrigid.csv and expX\_motionY\_imu\_rigid.csv, the header specifies

- 168         • the segment to which the IMU is attached,
- 169         • the accelerometer, gyroscope, and magnetometer readings,
- 170         • the x-/y-/z-component,

171     and it starts with seg1\_acc\_x, seg1\_acc\_y. For expX\_motionY\_omc.csv, the header specifies

- 172         • the segment to which the marker or estimated orientation belongs to,
- 173         • which of the four markers it is,
- 174         • the x-/y-/z-component (or u-/x-/y-/z- for quaternion),

175     and it starts with seg1\_marker1\_x, seg1\_marker1\_y.

176     For all .csv files, the sampling rate is specified as a comment in the first line, e.g., # sampling frequency: 40. All  
177     units are given in seconds/meters/radians or A.U. for the magnetometer. The numbering of segments (S1 to S5) and markers  
178     (M1 to M4) for both KCs (arm and gait) are given in Figure 5. Note that the sequence of types of motions that make up one  
179     experiment, they are from one continuous recording session, and as such, they can be concatenated to create a longer time  
180     series. Finally, we list the sequences of types of motions of all experiments.

- E01: canonical, pause1, slow1, pause2, fast, pause3, fast\_slow\_fast, freeze1, fast\_slow, freeze2, slow2, shaking, pause4
- E02: canonical1, pause1, slow\_fast\_mix, pause2, canonical2, pause3, slow\_fast\_freeze\_mix, pause4
- E03: slow1, dangle1, pause1, dangle2, pause2, slow2, dangle3, pause3, dangle4, pause4
- E04: slow\_global, pause1, fast\_global, pause2, dangle\_global1, pause3, dangle\_global2, pause4
- E05: pickandplace, pause
- E06: canonical, pause1, slow1, pause2, fast, pause3, fast\_slow\_fast, freeze1, fast\_slow, freeze2, slow2, pause4
- E07: canonical1, pause1, slow\_fast\_mix, pause2, canonical2, pause3, slow\_fast\_freeze\_mix, pause4
- E08: slow, dangle1, pause1, dangle2, pause2, dangle3, pause3, dangle4, pause
- E09: slow\_global, pause1, fast\_global, pause2, dangle\_global1, pause3, dangle\_global2, pause4
- E10: gait\_slow, gait\_fast, pause
- E11: quasistatic1, slow, rotation, shaking, quasistatic2, explosiv, pause

## 192 **Videos /videos/\* and Images /images/\***

193 The folder /videos/\* contains video recording of all experiments from two camera angles. For all eleven experiments,  
 194 the video files inside the folder are named expX\_camera1.mp4 and expX\_camera2.mp4. Additionally, there are rendered  
 195 videos of all experiments from three different perspectives and they are named expX\_render1.mp4, expX\_render2.mp4,  
 196 and expX\_render3.mp4. The folder /images/\* contains images of the KCs.

## 197 **Raw Data and Preprocessing Logic /make\_dataset/\***

198 For reproducibility, the folder /make\_dataset/raw\_data contains the raw data as it is recorded using the hardware of  
 199 the measurement setup. In combination with published data processing software, this allows any user to exactly reproduce the  
 200 processed dataset as it is published.

## 201 **CAD Files /cad\_files/\***

202 Additionally, we publish the files required for the 3D printing of the two five-segment KCs. The CAD files may be used to  
 203 3D-print new KCs and extend this dataset to include additional types of joints, motions, or combinations thereof.

## 204 **A Broad Range of Inertial Motion Tracking Problems**

205 The richness and versatility of the present dataset is showcased with the great amount of well-controlled IMTPs that can be  
 206 defined, by selecting specific combinations of the data, and thus varying the following aspects:

- *Types of Joints* (all 1D/2D/3D joints are available): Users of this dataset can create IMTPs that involve 1D, 2D, and/or 3D  
 207 joints by selecting specific segments. For 1D joints, x-, y-, and z-joint-axes directions are available. As a first step, users  
 208 identify the desired type of joint in Figure 5 and select the adjacent segment numbers. For example, for a two-segment  
 209 KC with a 2D joint, users have to choose the KC *gait*, and then can chose between the segments S2-S3 or S5-S1. For the  
 210 KC *gait*, users can then choose between E06 to E11 (e.g., see Table 1) and from all motions therein.
- *Length of KC* (can be varied up to a length of five segments): Users can create IMTPs that involve a single segment  
 211 or KCs of length two, three, four, or five segments. The desired sub-chains can be selected (Figure 5) and the desired  
 212 segment numbers can be identified.
- *Sparse Sensing* (every segment has IMU data available that may optionally be dropped): Users can create IMTPs that use  
 213 only a limited number of IMUs. This can be easily achieved by dropping the respective IMU measurements. For example,  
 214 for the tracking of a three-segment KC with double hinge joints, users can identify (Figure 5) that either S1-S2-S3 or  
 215 S2-S3-S4 are a suitable combination of segments, both from the KC *arm*. Then, users can choose between E01 to E05  
 216 and choose from any motion therein. Finally, to achieve sparse sensing the IMU measurements of the middle segment, so  
 217 either S2 or S3 are dropped.
- *Magnetometer-free Sensing*: Users can create IMTPs that do not make use of the magnetometer reading. This can be  
 218 achieved by simply dropping the magnetometer measurement.

- *Sensor-to-segment Alignment*: Users can choose to provide the joint-axes direction of 1D joints or not. These joint-axes direction have been validated to be accurate (see Technical Validation).
- *Types of Motions* (diverse set of performed motions): Users can select from a broad range of available motions as listed above.
- *Motion Artifacts*: Users can select between rigidly or nonrigidly attached IMUs for every segment. This choice has been validated to be significant (see Technical Validation).
- *Changing Setup*: Users can create a smooth transition between IMTPs, e.g., the transition between a non-sparse IMTP to a sparse IMTP. This can be relevant for, e.g., addressing dynamic changes in IMU configurations or IMU failures.
- *Trial Duration*: Users can select individual motions or concatenate several motions from one experiment to create a longer time series in a seamless way (without a non-smooth transition). This enables evaluating long-term stability.

### 233 Minor Irregularities in this Data Publication

234 For completion, we list all the minor irregularities in the provided data with this publication:

- 235 • Some of the experimental video recordings contained in the folder `/videos/*` are slightly out of focus.
- 236 • In experiment one (E01) the nonrigid IMU of segment three (S3) is very loosely attached and eventually flips over  
237 by 90 degrees along the longitudinal axis of the segment after five minutes and 25 seconds. Whilst inconsistent with  
238 the designed measurement protocol, this scenario opens up for evaluating the ability of IMT solutions to detect and  
239 compensate attachment loosening.

## 240 Technical Validation

241 In the following we validate the synchronization between the optical and inertial data, the sensor alignment, the mechanical  
242 validity of the joints' DoF, and investigate the effect of the foam attachment of IMUs by comparing their measurement signals  
243 to the signals from the rigidly-attached IMUs.

### 244 Validation of Time Synchronization

245 The OMC system and IMUs are time-synchronized in the following way: We first pinpoint the IMU data frame corresponding  
246 to OMC activation, and 2) trim the trailing portion of IMU data to match the length of the OMC time series. The optimal IMU  
247 frame coinciding with OMC activation is determined through cross-correlation between gyroscope and OMC measurements<sup>39</sup>.  
248 Table 2 lists for all experiments and all ten IMUs this optimal IMU frame. Since the ten IMUs are software time-synchronized,  
249 ideally, the optimal IMU frame should be consistent across IMUs. This is almost perfectly true for all experiments.

### 250 Validation of Alignment of Coordinate Systems

251 The rigidly-attached IMUs are attached to the segments such that each local sensor coordinate system  $\mathcal{S}$  is well aligned with the  
252 coordinate system  $\mathcal{B}$  of the segment to which the sensor is attached (see Figure 3). Because of this hardware alignment, the  
253 software alignment that is performed in the data processing (described in the methods section) should only report and correct  
254 a small remaining alignment error. The software alignment reports an average alignment correction of  $0.56 \pm 0.27$  degrees  
255 (averaged over all ten IMUs and all experiments). The largest reported alignment correction is 1.01 degrees.

### 256 Validation of Mechanical Hinge Joints and of Calibration

257 There are in total five 1D joints, mechanical hinge joints, in the two five-segment KCs. The KC *arm* has the x-, y-, and z-hinge  
258 joints, and the KC *gait* has two y-hinge joints (see Figure 5). The 3D printed setup, mechanical composition and other factors  
259 can introduce an error in the known directions of the axes and/or can lead to a slightly varying, non-constant rotation axes. For  
260 each hinge joint, we can propose a joint axis direction and then estimate the mean angle of the residual rotation (MARR), i.e.  
261 the rotation that is not around this joint axis direction. We achieve this by computing the relative orientation of the two adjacent  
262 segments for the chosen hinge joint from optical data, and then projecting this relative orientation into the rotational feasible  
263 subspace as defined by the proposed joint axis direction. The MARR is averaged over all available data for the chosen hinge  
264 joint. In addition, for each hinge joint, we can compute the MARR for the respective x-/y-/z-unit vectors, and we can find the  
265 optimal joint axis direction that minimizes the MARR. Both values are reported in Table 3. The optimized MARRs are low  
266 which validates that the mechanical construction of the 1D joints rotates nearly only around a constant joint axis direction. By  
267 comparing the MARR to the optimized MARR and observing that there is almost no difference, we can conclude that the joint  
268 axes directions are well calibrated.

## 269 Validation of Rigid and Nonrigid IMU Attachment

270 In order to assess the impact of the foam attachment of IMUs on the measured signals, we compare their power spectral  
271 density to the power spectral density of their rigidly-attached counterparts. The power spectral density is particularly suitable  
272 for identifying dominant frequencies and comparing the energy present in different frequency bands and it can be estimated  
273 numerically using the Welch's method<sup>40</sup>. Figure 6 shows the power spectral density over frequency for both accelerometer and  
274 gyroscope measurements, grouped by rigidly and foam-attached IMUs and averaged over all experimental data. We observe  
275 that the nonrigid attachment of IMUs does not result in a distinct or narrow range of disturbed frequencies. On the contrary, the  
276 entire mid-to-high frequency spectrum is affected. Therefore, there exists no special-purpose filtering approach to dampen the  
277 affected frequency range which justifies a generic approach based on a low-pass filter.

## 278 Usage Notes

279 To increase ease-of-use and aid fast adoption, we provide a lightweight Python package, titled diodem, that provides quick  
280 access to the data<sup>38</sup>. The Python package is hosted on PyPI and can be easily installed with `pip install imt-diodem`  
281 (requires Python  $\geq 3.10$ ). The source code of the Python package is hosted in a GitHub Repository (<https://github.com/SimiPixel/diodem>). The Python package exports only a single function `diodem.load_data`, and its usage is  
283 self-explanatory and is demonstrated in the following quick-start example.

```
1 import diodem
2
3 # concatenates 3 motions: the motion01, motion02 and motion03
4 # resample all data to 40 Hertz
5 data = diodem.load_data(
6     exp_id      = 1,
7     motion_start = 1,
8     motion_stop  = 3,
9     resample_to_hz = 40.0
10 )
11
12 print(data.keys())
13 # ['seg1', 'seg2', 'seg3', 'seg4', 'seg5']
14
15 print(data['seg1'].keys())
16 # ['imu_rigid', 'imu_nonrigid', 'marker1', 'marker2', 'marker3', 'marker4', 'quat']
17
18 print(data['seg1']['imu_rigid'].keys())
19 # ['acc', 'gyr', 'mag']
```

284 Additionally, the Python Package allows for easy resampling of the optical and inertial data to a common sampling rate. The  
285 following second code example showcases how the data for a three-segment, sparse KC with double hinge joints and y- and  
286 z-joint axes directions can be obtained. The task of this IMTP is to estimate the rotational state of the three-segment KC from  
287 two, rigidly-attached IMU measurements, attached on the two outer segments.

```
1 import diodem
2
3 # E01 to E05 can be used; they offer the KC `arm` with a sub-KC with double hinge joints and y- and
4 # z-joint axes directions
5 data = diodem.load_data(exp_id=1, resample_to_hz = 40.0)
6
7 # outer imu measurements
8 imu_seg_left, imu_seg_right = data['seg3']['imu_rigid'], data['seg5']['imu_rigid']
9
10 # ground truth orientations (as quaternions) from earth to body coordinate system
11 q_seg_left, q_seg_middle, q_seg_right = data['seg3']['quat'], data['seg4']['quat'],
12 # data['seg5']['quat']
```

## 288 Code availability

289 The raw inertial and optical data<sup>38</sup> was processed as outlined in the Methods Section (see Data Processing), and both raw  
290 data and the corresponding data processing software is made openly available. The processed dataset as it is published can be  
291 reconstructed by following the instructions in `/make_dataset/readme.md`. The published dataset was processed using  
292 the following dependencies: numpy 1.26.4, qmt 0.2.4, pandas 2.2.1, scipy 1.12.0, dm-tree 0.1.8.

## 293 References

- 294 1. Picerno, P. *et al.* Wearable inertial sensors for human movement analysis: a five-year update. *Expert. Rev. Med. Devices* **2021**, *18*, 79–94, [10.1080/17434440.2021.1988849](https://doi.org/10.1080/17434440.2021.1988849) (2021). PMID: 34601995, <https://doi.org/10.1080/17434440.2021.1988849>.
- 295 2. García-de Villa, S., Casillas-Pérez, D., Jiménez-Martín, A. & García-Domínguez, J. J. Inertial sensors for human motion  
296 analysis: A comprehensive review. *IEEE Transactions on Instrumentation Meas.* **2023**, *72*, 1–39, [10.1109/TIM.2023.3276528](https://doi.org/10.1109/TIM.2023.3276528)  
297 (2023).
- 298 3. Dafarra, S. *et al.* icub3 avatar system: Enabling remote fully immersive embodiment of humanoid robots. *Sci. Robotics* **2024**, *9*,  
299 eadh3834, [10.1126/scirobotics.adh3834](https://doi.org/10.1126/scirobotics.adh3834) (2024).
- 300 4. Cinnera, A. M. *et al.* Upper limb assessment with inertial measurement units according to the international classification  
301 of functioning in stroke: a systematic review and correlation meta-analysis. *Top. Stroke Rehabil.* **2024**, *31*, 66–85, [10.1080/10749357.2023.2197278](https://doi.org/10.1080/10749357.2023.2197278) (2024).
- 301 5. Zhao, M. *et al.* Design, modeling, and control of an aerial robot dragon: A dual-rotor-embedded multilink robot with the  
302 ability of multi-degree-of-freedom aerial transformation. *IEEE Robotics Autom. Lett.* **2018**, *3*, 1176–1183, [10.1109/LRA.2018.2793344](https://doi.org/10.1109/LRA.2018.2793344) (2018).
- 303 6. Kanko, R. M., Laende, E. K., Davis, E. M., Selbie, W. S. & Deluzio, K. J. Concurrent assessment of gait kinematics using  
304 marker-based and markerless motion capture. *J. Biomech.* **2021**, *127*, 110665, [http://dx.doi.org/10.1016/j.jbiomech.2021.110665](https://doi.org/10.1016/j.jbiomech.2021.110665)  
305 (2021).
- 306 7. Uhlrich, S. D. *et al.* OpenCap: Human movement dynamics from smartphone videos. *PLOS Comput. Biol.* **2023**, *19*, 1–26,  
307 [http://dx.doi.org/10.1371/journal.pcbi.1011462](https://doi.org/10.1371/journal.pcbi.1011462) (2023).
- 308 8. Weber, D., Gühmann, C. & Seel, T. RIANN—A Robust Neural Network Outperforms Attitude Estimation Filters. *AI* **2021**, *2*,  
309 444–463, [10.3390/ai2030028](https://doi.org/10.3390/ai2030028) (2021).
- 310 9. Laidig, D., Weygers, I., Bachhuber, S. & Seel, T. VQF: A Milestone in Accuracy and Versatility of 6D and 9D Inertial  
311 Orientation Estimation. In *2022 25th International Conference on Information Fusion (FUSION)*, 1–6, [10.23919/FUSION49751.2022.9841356](https://doi.org/10.23919/FUSION49751.2022.9841356) (2022).
- 312 10. Subbu, K. P., Gozick, B. & Dantu, R. LocateMe: Magnetic-fields-based indoor localization using smartphones. *ACM Trans. Intell. Syst. Technol.* **2013**, *4*, 73:1–73:27, [10.1145/2508037.2508054](https://doi.org/10.1145/2508037.2508054) (2013).
- 313 11. de Vries, W. H. K., Veeger, H. E. J., Baten, C. T. M. & van der Helm, F. C. T. Magnetic distortion in motion labs,  
314 implications for validating inertial magnetic sensors. *Gait & Posture* **2009**, *29*, 535–541, [10.1016/j.gaitpost.2008.12.004](https://doi.org/10.1016/j.gaitpost.2008.12.004) (2009).
- 315 12. Laidig, D., Weygers, I. & Seel, T. Self-Calibrating Magnetometer-Free Inertial Motion Tracking of 2-DoF Joints. *Sensors*  
316 **2022**, *22*, 9850, [10.3390/s22249850](https://doi.org/10.3390/s22249850) (2022).
- 317 13. Köhler, J., Invernizzi, M., Haan, P. D. & Noe, F. Rigid Body Flows for Sampling Molecular Crystal Structures. In  
318 *Proceedings of the 40th International Conference on Machine Learning*, 17301–17326 (PMLR, 2023).
- 319 14. Lehmann, D., Laidig, D., Bachhuber, S., Seel, T. & Weygers, I. Magnetometer-free inertial motion tracking of kinematic  
320 chains, [10.2139/ssrn.4785077](https://doi.org/10.2139/ssrn.4785077) (2024).
- 321 15. Seel, T., Raisch, J. & Schauer, T. Imu-based joint angle measurement for gait analysis. *Sensors* **2014**, *14*, 6891–6909,  
322 [10.3390/s140406891](https://doi.org/10.3390/s140406891) (2014).
- 323 16. McGrath, T., Fineman, R. & Stirling, L. An Auto-Calibrating Knee Flexion-Extension Axis Estimator Using Principal  
324 Component Analysis with Inertial Sensors. *Sensors* **2018**, *18*, 1882, [10.3390/s18061882](https://doi.org/10.3390/s18061882) (2018).
- 325 17. Olsson, F., Kok, M., Seel, T. & Halvorsen, K. Robust Plug-and-Play Joint Axis Estimation Using Inertial Sensors. *Sensors*  
326 **2020**, *20*, 3534, [10.3390/s20123534](https://doi.org/10.3390/s20123534) (2020).
- 327 18. Weenk, D., Van Beijnum, B.-J. F., Baten, C. T., Hermens, H. J. & Veltink, P. H. Automatic identification of inertial sensor  
328 placement on human body segments during walking. *J. neuroengineering rehabilitation* **2013**, *10*, 1–9, [10.1186/1743-0003-10-31](https://doi.org/10.1186/1743-0003-10-31)  
329 (2013).
- 330 19. Nazarabari, M. & Rouhani, H. Semi-automatic sensor-to-body calibration of inertial sensors on lower limb using gait  
331 recording. *IEEE Sensors J.* **2019**, *19*, 12465–12474, [10.1109/JSEN.2019.2939981](https://doi.org/10.1109/JSEN.2019.2939981) (2019).
- 332 20. Taetz, B., Lorenz, M., Miezal, M., Stricker, D. & Bleser-Taetz, G. Jointtracker: Real-time inertial kinematic chain  
333 tracking with joint position estimation [version 1; peer review: 1 approved with reservations]. *Open Res. Eur.* **2024**, *4*,  
334 [10.12688/openreseurope.16939.1](https://doi.org/10.12688/openreseurope.16939.1) (2024).

- 341 21. Bachhuber, S. *et al.* Plug-and-Play Sparse Inertial Motion Tracking With Sim-to-Real Transfer. *IEEE Sensors Lett.* **7**, 1–4,  
342 [10.1109/LSENS.2023.3307122](https://doi.org/10.1109/LSENS.2023.3307122) (2023).
- 343 22. Eckhoff, K., Kok, M., Lucia, S. & Seel, T. Sparse magnetometer-free inertial motion tracking – a condition for observability  
344 in double hinge joint systems. *IFAC-PapersOnLine* **53**, 16023–16030, [10.1016/j.ifacol.2020.12.403](https://doi.org/10.1016/j.ifacol.2020.12.403) (2020). 21st IFAC  
345 World Congress.
- 346 23. Dorschky, E. *et al.* Comparing sparse inertial sensor setups for sagittal-plane walking and running reconstructions. *bioRxiv*  
347 2023–05, [10.1101/2023.05.25.542228](https://doi.org/10.1101/2023.05.25.542228) (2023).
- 348 24. Forner-Cordero, A. *et al.* Study of the motion artefacts of skin-mounted inertial sensors under different attachment  
349 conditions. *Physiol. Meas.* **29**, N21, [10.1088/0967-3334/29/4/N01](https://doi.org/10.1088/0967-3334/29/4/N01) (2008).
- 350 25. Remmerswaal, E., Weygers, I., Smit, G. & Kok, M. Fast relative sensor orientation estimation in the presence of real-world  
351 disturbances. In *2021 European Control Conference (ECC)*, 411–416, [10.23919/ECC54610.2021.9654849](https://doi.org/10.23919/ECC54610.2021.9654849) (2021).
- 352 26. Palermo, M., Cerqueira, S. M., André, J., Pereira, A. & Santos, C. P. From raw measurements to human pose—a dataset  
353 with low-cost and high-end inertial-magnetic sensor data. *Sci. Data* **9**, 591, [10.1038/s41597-022-01690-y](https://doi.org/10.1038/s41597-022-01690-y) (2022).
- 354 27. Jayasinghe, U., Hwang, F. & Harwin, W. S. Inertial measurement data from loose clothing worn on the lower body during  
355 everyday activities. *Sci. Data* **10**, 709, [10.1038/s41597-023-02567-4](https://doi.org/10.1038/s41597-023-02567-4) (2023).
- 356 28. Konak, O. *et al.* Sonar, a nursing activity dataset with inertial sensors. *Sci. data* **10**, 727, [10.1038/s41597-023-02620-2](https://doi.org/10.1038/s41597-023-02620-2)  
357 (2023).
- 358 29. García-de Villa, S. *et al.* A database with frailty, functional and inertial gait metrics for the research of fall causes in older  
359 adults. *Sci. Data* **10**, 566, [10.1038/s41597-023-02428-0](https://doi.org/10.1038/s41597-023-02428-0) (2023).
- 360 30. Seong, M. *et al.* Multisensebadminton: Wearable sensor-based biomechanical dataset for evaluation of badminton  
361 performance. *Sci. Data* **11**, 343, [10.1038/s41597-024-03144-z](https://doi.org/10.1038/s41597-024-03144-z) (2024).
- 362 31. Dong, A. *et al.* A new kinematic dataset of lower limbs action for balance testing. *Sci. data* **10**, 209, [10.1038/s41597-023-02105-2](https://doi.org/10.1038/s41597-023-02105-2) (2023).
- 363 32. Santos, G., Wanderley, M., Tavares, T. & Rocha, A. A multi-sensor human gait dataset captured through an optical system  
364 and inertial measurement units. *Sci. Data* **9**, 545, [10.1038/s41597-022-01638-2](https://doi.org/10.1038/s41597-022-01638-2) (2022).
- 365 33. Mehdizadeh, S. *et al.* The toronto older adults gait archive: video and 3d inertial motion capture data of older adults’  
366 walking. *Sci. data* **9**, 398, [10.1038/s41597-022-01495-z](https://doi.org/10.1038/s41597-022-01495-z) (2022).
- 367 34. Cognolato, M. *et al.* Gaze, visual, myoelectric, and inertial data of grasps for intelligent prosthetics. *Sci. data* **7**, 43,  
368 [10.1038/s41597-020-0380-3](https://doi.org/10.1038/s41597-020-0380-3) (2020).
- 369 35. Grouvel, G., Carcreff, L., Moissenet, F. & Armand, S. A dataset of asymptomatic human gait and movements obtained  
370 from markers, imus, insoles and force plates. *Sci. Data* **10**, 180, [10.1038/s41597-023-02077-3](https://doi.org/10.1038/s41597-023-02077-3) (2023).
- 371 36. Weygers, I. *et al.* Reference in-vitro dataset for inertial-sensor-to-bone alignment applied to the tibiofemoral joint. *Sci.  
372 Data* **8**, 208 (2021).
- 373 37. Szczęsna, A. *et al.* Reference data set for accuracy evaluation of orientation estimation algorithms for inertial motion  
374 capture systems. vol. 9972, 509–520, [10.1007/978-3-319-46418-3\\_45](https://doi.org/10.1007/978-3-319-46418-3_45) (2016).
- 375 38. Bachhuber, S., Lehmann, D., Weygers, I. & Seel, T. DIODEM – A Diverse Inertial and Optical Dataset of kinEmatic chain  
376 Motion, [10.7910/DVN/SGJLZA](https://doi.org/10.7910/DVN/SGJLZA) (2024).
- 377 39. Laidig, D., Caruso, M., Cereatti, A. & Seel, T. BROAD—A Benchmark for Robust Inertial Orientation Estimation. *Data* **6**,  
378 72, [10.3390/data6070072](https://doi.org/10.3390/data6070072) (2021).
- 379 40. Welch, P. The use of fast fourier transform for the estimation of power spectra: A method based on time averaging over  
380 short, modified periodograms. *IEEE Transactions on Audio Electroacoustics* **15**, 70–73, [10.1109/TAU.1967.1161901](https://doi.org/10.1109/TAU.1967.1161901)  
381 (1967).
- 382

## 383 Acknowledgements

384 There are no non-author acknowledgements to mention.

## 385 Author contributions statement

386 S.B. and D.L. contributed equally to this work. D.L. designed and built the kinematic chains. S.B. and D.L. and T.S. conceived  
387 the experiments. S.B. and D.L. and T.S. conducted the experiments. S.B. and D.L. processed the data. S.B. and D.L. and I.W.  
388 drafted, wrote and formatted the manuscript. All authors reviewed the manuscript.

389 **Competing interests**

390 The authors declare no competing interests.

391 **Figures & Tables**

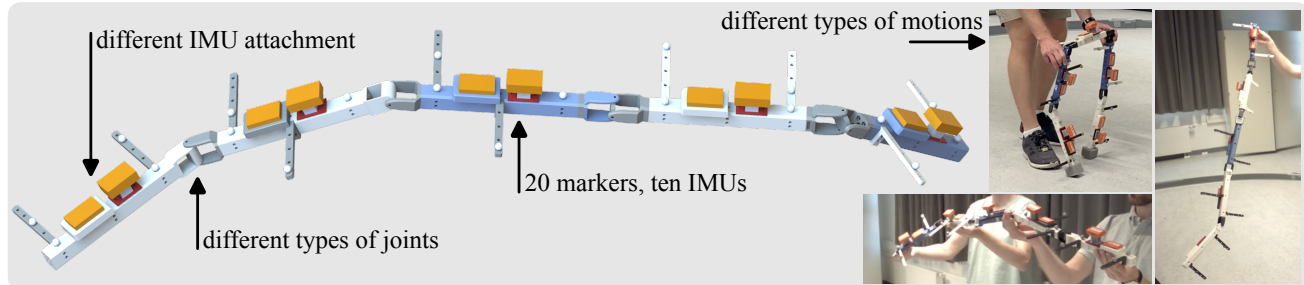


**Figure 1.** This dataset contains optical and inertial data of five-segment Kinematic Chains (KCs) that perform motions of various speeds and characteristics. This figure shows the CAD model of one of the experimental 3D-printed five-segment KC, titled arm, with ten IMUs (orange boxes) and 20 optical motion capture markers (gray spheres). The KC uses three hinge joints, each oriented along the z, y, and x axes, respectively, followed by a spherical joint. In addition, the types of joints can be modified to create a second distinctive five-segment KC, titled gait, and experimental trials have been conducted for both KCs. All segments of both KCs are equipped with two IMUs: one firmly attached to the segment and another affixed nonrigidly using foam padding.



**Figure 2.** Each segment of both five-segment KCs is equipped with two IMUs: one firmly attached to the segment and another affixed nonrigidly using foam padding. The foam padding allows for relative motion between the segment and the sensor, which creates motion artifacts, and its compensation requires advanced IMT solutions.

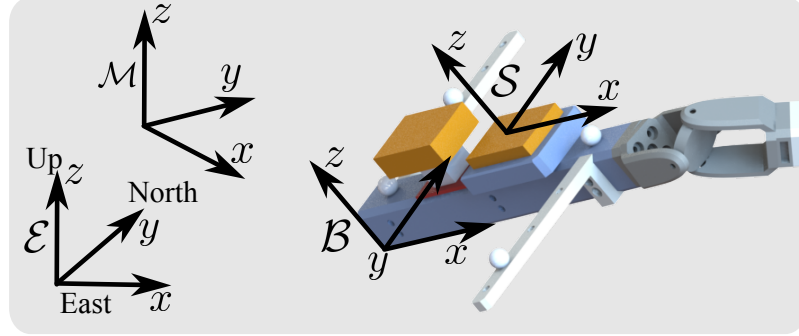


**Figure 3.** Definitions of the different local coordinate systems and reference coordinate systems. IMT methods use the IMU data (orange boxes) as measured in the local sensor coordinate system  $\mathcal{S}$  to estimate the orientation of the local sensor coordinate system relative to the earth reference coordinate system  $\mathcal{E}$  with an x-axis pointing towards east, a y-axis pointing to the magnetic north, and a z-axis pointing upwards. The OMC system tracks the 3D position of the markers (white spheres) relative to the OMC’s reference coordinate system  $\mathcal{M}$ . The markers are rigidly attached to the segment and their 3D position trajectories can be used to span an orthogonal coordinate system for the segment (or body)  $\mathcal{B}$ .

**Table 1.** Summary of processed dataset. In total, eleven experiments are obtained. Five experiments use the five-segment KC arm and six experiments use the five-segment KC gait. Each experiment is typically several minutes in duration and consists of various types of motions. For all experiments and all motions therein, the same extensive inertial and optical data is available<sup>38</sup> which consists of ten 9D (3D accelerometer, 3D gyroscope, 3D magnetometer) IMUs, 20 3D OMC marker trajectories, and five OMC orientation trajectories. Additionally, for documentation purpose, there is video recording at all times from two camera angles.

Experiment →	E01	E02	E03	E04	E05	E06	E07	E08	E09	E10	E11	$\Sigma$
KC	Arm	Arm	Arm	Arm	Arm	Gait	Gait	Gait	Gait	Gait	Gait	2
Duration [seconds]	368	350	275	207	80	294	359	277	212	151	205	2778
Number of Motions	13	8	10	8	2	12	8	9	8	3	7	88

**Table 2.** IMU Frame Offset Across Experiments

Experiment →	E01	E02	E03	E04	E05	E06	E07	E08	E09	E10	E11
IMU 9F	156	112	124	121	107	90	102	96	118	155	70
IMU B8	156	112	124	122	107	92	102	96	118	155	70
IMU A3	156	112	124	121	107	90	102	96	118	155	70
IMU 84	156	112	124	122	108	91	102	96	118	155	70
IMU A0	156	112	124	122	107	91	102	96	118	155	70
IMU A2	156	112	125	121	107	91	102	95	118	156	70
IMU A4	156	112	124	121	107	90	102	96	118	155	70
IMU 9B	156	112	124	122	107	92	102	96	118	156	70
IMU 99	156	112	124	122	107	92	102	96	118	155	70
IMU 85	156	112	124	121	107	91	102	96	118	156	70

**Table 3.** Mean Angle of Residual Rotation (MARR) for all experimental hinge joints and for both major and optimized joint axis direction. Ideally, the MARR should be zero, as it would imply a perfect 1-DoF joint.

Hinge Joint	Axis Direction	MARR [deg]	Optimized MARR [deg]
KC Arm: Between S2 and S3	$(1, 0, 0)^T$	$3.44 \pm 1.41$	$3.42 \pm 1.42$
KC Arm: Between S3 and S4	$(0, 1, 0)^T$	$0.98 \pm 0.99$	$0.98 \pm 1.00$
KC Arm: Between S4 and S5	$(0, 0, 1)^T$	$0.57 \pm 1.79$	$0.55 \pm 1.79$
KC Gait: Between S5 and S1	$(0, 1, 0)^T$	$1.69 \pm 3.22$	$1.63 \pm 3.22$
KC Gait: Between S3 and S4	$(0, 1, 0)^T$	$0.98 \pm 0.58$	$0.95 \pm 0.60$

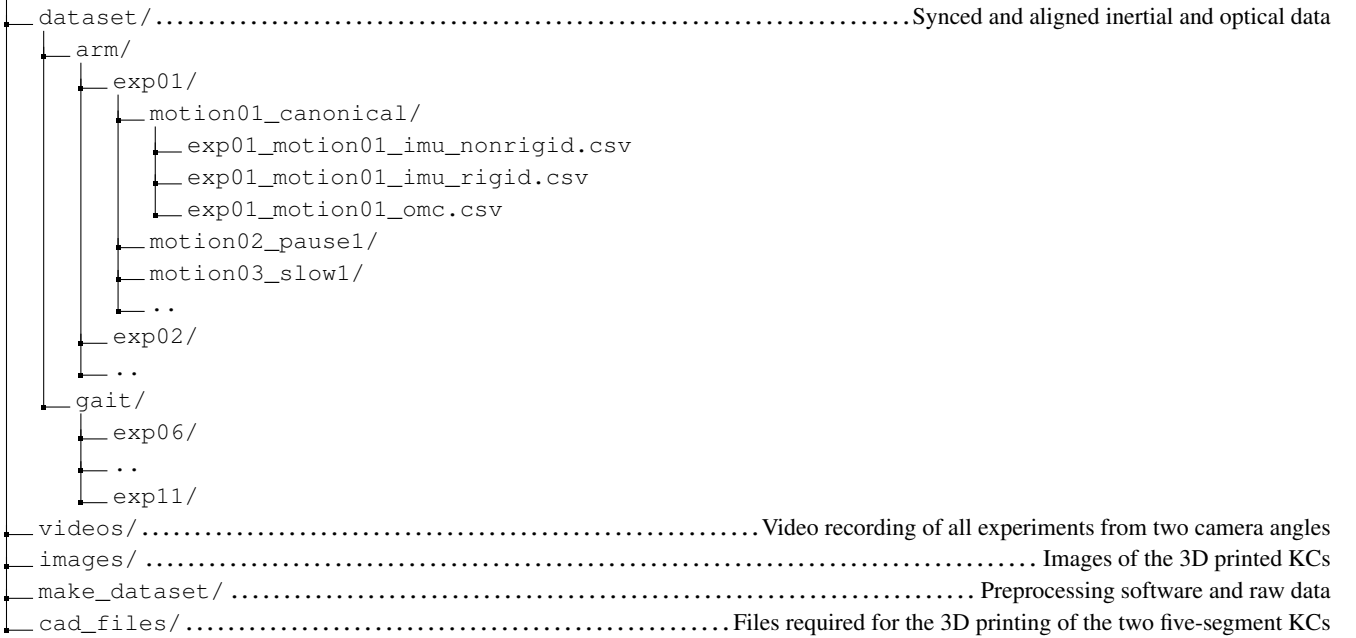


**Figure 4.** Visualization of the folder structure of the data records<sup>38</sup>. The data records include 1) the (processed) dataset, 2) associated videos of the experiments and images of the KCs, 3) the corresponding raw data and data processing software and tools employed, and 4) the CAD files for 3D-printing the KCs.

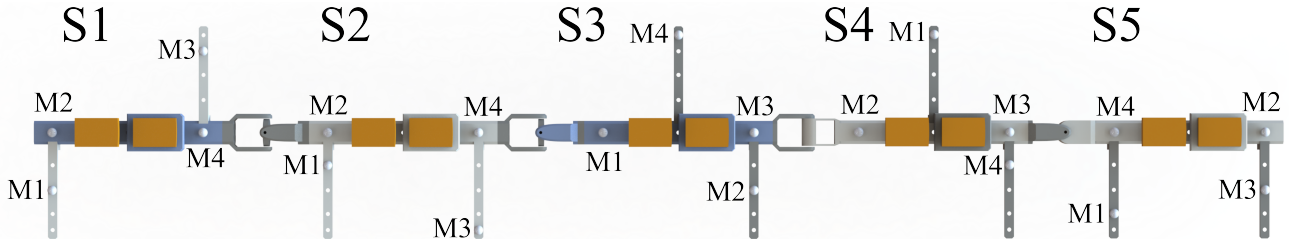


**Figure 5.** The numbering of segments (S1 to S5) and markers (M1 to M4) here given for the KC *arm* (used in experiments one to five). The types of joints for the KC *arm* (from left to right) are spherical, hinge-x, hinge-y, and hinge-z. The second KC *gait* (used in experiments six to eleven) consists of the segments (from left to right) S5-S1-S2-S3-S4 with the types of joints hinge-y, saddle, saddle, and hinge-y. The marker numbers for each segment are the same for KC *arm* and *gait*.

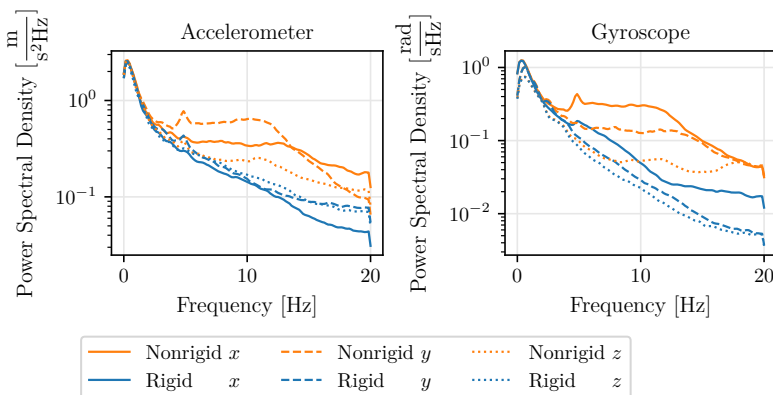


**Figure 6.** The impact of the foam-attachment of IMUs on the spectral density of the measured signals. Averaged over  $\approx 4$  hours of IMU data. We observe that the nonrigid attachment of IMUs does not result in a distinct or narrow range of disturbed frequencies.